Sub-1 K adiabatic demagnetization refrigeration with rare-earth borates Ba3XB9O18 and Ba3XB3O9, X = (Yb, Gd)

Marvin Klinger, Tim Treu, Felix Kreisberger, Christian Heil, Anna Klinger, Anton Jesche, Philipp Gegenwart

Klinger, Marvin, Tim Treu, Felix Kreisberger, Christian Heil, Anna Klinger, Anton Jesche, and Philipp Gegenwart. 2025. "Sub-1 K adiabatic demagnetization refrigeration with rare-earth borates Ba3XB9O18 and Ba3XB3O9, X = (Yb, Gd)." Applied Sciences 16 (1): 290. https://doi.org/10.3390/app16010290.

applied sciences

Article

Sub-1 K Adiabatic Demagnetization Refrigeration with Rare-Earth Borates $Ba_3XB_9O_{18}$ and $Ba_3XB_3O_9$, X = (Yb, Gd)

Marvin Klinger, Tim Treu, Felix Kreisberger, Christian Heil, Anna Klinger, Anton Jesche and Philipp Gegenwart *

Experimental Physics VI, Center for Electronic Correlations and Magnetism, Institute of Physics, University of Augsburg, 86159 Augsburg, Germany; marvin.klinger@physik.uni-augsburg.de (M.K.)
* Correspondence: philipp.gegenwart@physik.uni-augsburg.de

Featured Application

The materials studied in this work can be utilized for adiabatic demagnetization refrigeration down to the milli-Kelvin range and offer multiple benefits over traditional hydrated paramagnetic salts.

Abstract

Adiabatic demagnetization refrigeration (ADR) is regaining relevance for refrigeration to temperatures below 1 K as global helium-3 supply is increasingly strained. While ADR at these temperatures is long established with paramagnetic hydrated salts, more recently, frustrated rare-earth oxides were found to offer higher entropy densities and practical advantages, since they do not degrade under heating or evacuation. We report structural, magnetic, and thermodynamic properties of the rare-earth borates $Ba_3XB_9O_{18}$ and $Ba_3XB_3O_9$ with X = (Yb, Gd). Except for $Ba_3GdB_9O_{18}$, which orders at 108 mK, the three other materials remain paramagnetic down to their lowest measured temperatures. ADR performance starting at 2 K in a field of 5 T is analyzed and compared to literature.

Keywords: adiabatic demagnetization refrigeration; magnetocaloric effect; sub-Kelvin temperature; magnetic order; frustration

1. Introduction

Temperatures below one Kelvin are increasingly utilized not only in basic research but also in a growing number of industrial applications [1]. While dilution refrigerators (DRs) have long been the default option for obtaining and maintaining low temperatures [2,3], there have been recent advances and renewed interest in ADR [4–7]. These can be grouped into two broad categories: refrigerator technology and refrigerant technology.

In terms of refrigerator technology, there have been developments in continuous ADR that can maintain a set temperature by cycling multiple refrigerators connected via heat switches. While such setups are more complex than single-shot ADR, they offer the crucial benefit of maintaining continuous operation of the cold payload [8–10]. At the moment, continuous ADR is not yet competitive with DRs in terms of cooling power [11].

The field of refrigerant technology has long been limited by the performance characteristics of paramagnetic hydrated salts. Here, a large distance between magnetic moments, achieved by separating them with water molecules, achieves very weak magnetic interaction and correspondingly low ordering temperatures. As a consequence, the magnetic

Check for updates

Academic Editor: Israel Felner

Received: 8 December 2025
Revised: 23 December 2025
Accepted: 25 December 2025
Published: 27 December 2025

https://doi.org/10.3390/app16010290

entropy density and the cooling power are low. Furthermore, due to their chemical instability, paramagnetic hydrated salts like ferric ammonium alum, cerium magnesium nitrate, and others need to be encapsulated for use in a vacuum environment, and even then they may never be heated above room temperature. Otherwise, the crystal water contained in these substances will quickly escape, and structural collapse will make them inoperative for ADR.

There have been three major development avenues for new refrigerants with higher entropy density and better chemical stability: Single-crystal refrigerants like gadolinium gallium garnet or ytterbium gallium garnet offer high entropy density and allow ADR to 1 and 0.2 K, respectively [12–14]. Intermetallic compounds like $YbNi_{1.6}Sn$ have a much higher thermal conductivity because of the conduction electron contribution, while maintaining a high entropy density, and are thus a suitable alternative at temperatures down to 0.2 K [15–18]. The third alternative is rare-earth oxides in which geometrical frustration reduces the ordering temperature, allowing much lower ADR end temperatures in combination with a high entropy density [19–33]. These materials are chemically stable, the polycrystal synthesis can easily be upscaled, and excellent thermal and mechanical properties are obtained by compressing them with fine silver powder admixture, while maintaining a relatively high entropy density. Prototypes of this new class of oxide ADR materials include the borates $KBaX(BO_3)_2$ with magnetic triangular lattices of X = Yb, Gd [34,35]. While $KBaGd(BO_3)_2$ orders antiferromagnetically at 263 mK, the ADR experiment on a pellet in the Quantum Design Physical Property Measurement System (PPMS), starting at 2 K in a field of 5 T, revealed a minimal temperature of 122 mK [20]. Assuming a scaling of the ordering temperatures by the square of the ratio of the saturation moments (which is about 30), for isostructural $KBaYb(BO_3)_2$, a very low ordering near 9 mK has been deduced, and indeed, the system remains paramagnetic in ADR experiments down to 16 mK [19]. This is much lower than the minimal temperatures that can be obtained with the metallic ADR materials mentioned above. Both geometrical frustration due to the triangular magnetic lattice and K^+/Ba^{2+} site randomness [34] may be important with respect to the outstanding ADR performance of the two materials [20].

$Ba_3YbB_3O_9$ is another triangular lattice ADR candidate material with a very similar intralayer Yb-Yb distance (5.43 Å) as in $KBaYb(BO_3)_2$, but an about 30% larger interlayer Yb-Yb distance [36–39], making it more two-dimensional. Furthermore, $Ba_3YbB_3O_9$ has no site randomness, but it does exhibit two inequivalent Yb sites. We also study the triangular lattice material $Ba_3YbB_9O_{18}$, with a significantly larger in-plane Yb-Yb distance of 7.18 Å, which arises from a larger separation of YbO_6 octahedra by the triangular arrangement of the BO_3 groups in the structure [39–41]. It is interesting to compare the ADR performance of these materials, together with their Gd counterparts, to that of $KBaX(BO_3)_2$ (X=Yb, Gd). In the Gd variants with classical spin $S = 7/2$, the higher entropy density improves ADR performance at the expense of minimal ADR temperature, due to the enhanced magnetic couplings.

The rest of this paper is organized as follows: After the description of the utilized methods, we report below structural, magnetic, thermodynamic, and ADR properties of $Ba_3XB_9O_{18}$ and $Ba_3XB_3O_9$ with X = (Yb, Gd). No indication of magnetic ordering has been found in either of these Yb compounds down to the lowest obtained ADR temperatures of below 40 mK. In $Ba_3GdB_3O_9$, a broad maximum is found at low temperatures. In $Ba_3GdB_9O_{18}$, a Schottky-type broad peak, as well as a sharp phase transition, indicative of long-range magnetic order at lower temperatures, is observed in the heat capacity.

2. Materials and Methods

Polycrystals of $Ba_3XB_9O_{18}$ and $Ba_3XB_3O_9$ with X = (Yb, Gd) were prepared by solid-state reaction. The precursors were X_2O_3, $BaCO_3$, and H_3BO_3 with a purity of at least 99.9%. To compensate for losses, an excess of 2% wt. $BaCO_3$ and 4% wt. H_3BO_3 was used. All reagents were preheated, weighed, and thoroughly ground in an agate mortar. Subsequently, they were preheated in a furnace under a laboratory atmosphere at 700 °C over 12 h. After the first furnace run, the reagents were allowed to cool and then reground. A second oven run was performed under a laboratory atmosphere, but this time with an increased temperature of 900 °C over 24 h.

The products were ground again and analyzed for phase purity by powder X-ray diffraction in a PANAlytical Empyrean XRD (Almelo, Netherlands). To ensure good thermal contact, even at very low temperatures, the substances were mixed with 50% silver powder by weight and pressed into pellets for further analysis.

Pellets of 3 mm diameter were prepared for specific heat and magnetization measurements, while 15 mm diameter pellets were prepared for direct magnetocaloric studies.

Magnetization was measured in a Quantum Design MPMS3 SQUID magnetometer (San Diego, CA, USA); for measurements in the range $0.4\,\mathrm{K} < T < 2\,\mathrm{K}$, the ^{3}He option was utilized. The samples' magnetic moment was measured under an isothermal field sweep with a vibrating-sample magnetometer (VSM). In order to achieve higher accuracy, DC magnetization measurements were conducted at the initial and final fields, and the VSM data was scaled to these DC measurements. Furthermore, the data was corrected for the calculated geometry factor of the cylindrical samples.

Specific heat was measured in a PPMS DynaCool by Quantum Design (San Diego, CA, USA). For measurements at lower temperatures, a ^{3}He upgrade was utilized, for which a small piece was cut from the middle of a 3 mm pellet in order to limit the total specific heat and, thus, allow for more accurate and faster measurements.

The actual ADR performance of the samples was determined in a custom-built adiabatic demagnetization refrigeration setup inside a PPMS similar to the ones described in [19–21,25]. This setup comprises a standard PPMS puck that mounts a polyimide (PI) frame in which the pellet is supported by aromatic polyamide yarns. The suspended pellet is shielded from infrared radiation by a polished brass cap. Thermometry in this setup is performed by an ultra-low specific heat, low-time constant custom chip thermometer made from a commercially available RuO_2 chip resistor by removing the contacts and substrate. This thermometer was calibrated against a reference thermometer and attached to the pellet with GE 7031 varnish. Care was taken so as not to overheat the thermometer. Thus, the excitation was limited to less than 50 fW. Similarly a heater was prepared from a lower-resistance chip and also attached to the pellet. To limit thermal flux into the sample, superconducting wiring was utilized.

3. Results

3.1. Structure

Powder X-ray diffraction (PXRD) was performed at room temperature with a PANAlytical Empyrean diffractometer. The diffraction patterns were compared to the ICCD PDF-5+ database [42–44], and Rietveld refinements were conducted to determine phase purity. All samples contained only small fractions of foreign phases, of which the most common were identified as the corresponding rare-earth borates $(\mathrm{Yb},\mathrm{Gd})BO_3$. Elevated concentrations of a foreign phase were found in $Ba_3YbB_9O_{18}$ at 1.2% wt. $YbBO_3$ and in $Ba_3GdB_9O_{18}$ at 1.1% wt. $GdBO_3$. A central peak at 44.5° can be attributed to the sample holder.

Both $Ba_3YbB_9O_{18}$ and $Ba_3GdB_9O_{18}$ form a hexagonal lattice of identical space group $P6_3/m$ with one rare-earth site forming layers in the *ab* plane (Figure 1B,D). The rare-earth ions are coordinated in a hexagonal fashion, allowing for geometric frustration [36,37]. The layers differ by alternating orientations of the oxygen octahedra, further enhancing interlayer frustrations.

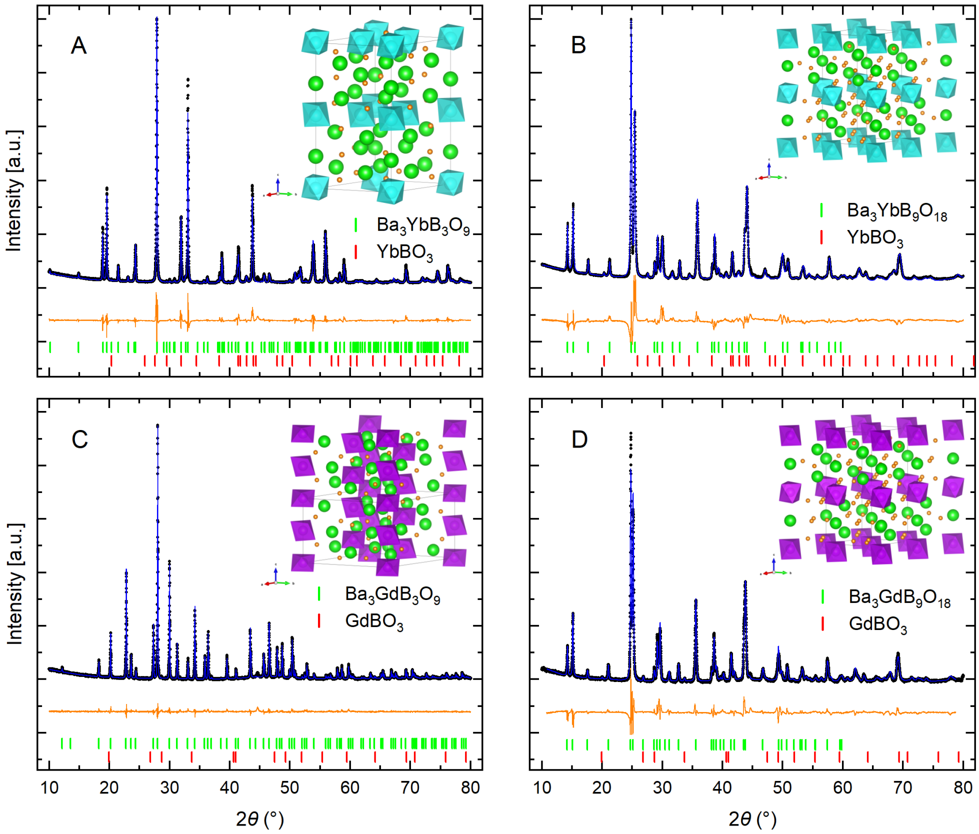

Figure 1. PXRD data (black) and literature peak positions for the product (green), as well as the most common foreign phase (red), Rietveld refinement (blue), and error (orange) for $Ba_3YbB_3O_9$ (**A**), $Ba_3YbB_9O_{18}$ (**B**), $Ba_3GdB_3O_9$ (**C**), and $Ba_3GdB_9O_{18}$ (**D**). The insets show the crystal structures with rare-earth ions surrounded by oxygen octahedra (Yb: blue, Gd: purple) and separated by boron (orange) and barium (green). Oxygen atoms have been omitted for clarity, and solid lines represent unit cells.

$Ba_3YbB_3O_9$ forms a hexagonal lattice of space group $P6_3cm$ [39]. In this compound, the ytterbium ions also form layers in the *ab* plane; however, these layers contain two alternating Yb sites and are distorted (Figure 1A). The two sites share the orientation of the oxygen octahedra, and the layers differ by alternating orientations of the octahedra along the *c* axis. This arrangement allows for additional frustration between the two distinct Yb sites. A similar structure has been observed for $Ba_3TbB_3O_9$ [45].

$Ba_3GdB_3O_9$ exhibits major differences to the other compounds. It crystallizes in a trigonal lattice ($R\bar{3}$) with two distinct gadolinium sites forming alternating chains along the *c* axis (Figure 1C). These chains are separated from each other with nearest-neighbor chains offset along *c*. Similar structures have been known to harbor a manifold of magnetic phases in other substances [46,47]. There is little literature available on $Ba_3GdB_3O_9$ except for the structure, which we confirmed by PXRD [42]. The relevant parameters are listed in Table 1. The distance between the (next) nearest neighbors governs the interaction between the rare-earth ions' magnetic moments; thus, these parameters are listed in Table 2.

Table 1. Structural data for the compounds, verified by powder XRD.

Compound	Lattice	Space Group	Unit Cell Parameters	Molar Volume
$Ba_3YbB_9O_{18}$ [42]	Hexagonal	$P6_3/m$	a: 7.1740 Å, c: 16.915 Å	227.0 cm^3 mol^{-1}
$Ba_3YbB_3O_9$ [43]	Hexagonal	$P6_3/cm$	a: 9.3830 Å, c: 17.441 Å	133.5 cm^3 mol^{-1}
$Ba_3GdB_9O_{18}$ [42]	Hexagonal	$P6_3/m$	a: 7.1934 Å, c: 17.206 Å	232.2 cm^3 mol^{-1}
$Ba_3GdB_3O_9$ [44]	Trigonal	$R\bar{3}$	a: 12.776 Å, c: 9.6063 Å	141.8 cm^3 mol^{-1}

Table 2. Distance between magnetic moments, verified by powder XRD. Parameters for the phonon contribution to the specific heat are listed as Einstein and Debye temperatures, as well as a mixing factor γ.

Compound	Nearest Neighbor (NN)	Next NN	Θ_E	Θ_D	γ
$Ba_3YbB_9O_{18}$ [42]	7.174 Å	8.458 Å	292 K	148 K	0.85
$Ba_3YbB_3O_9$ [43]	5.417 Å	8.721 Å	89 K	364 K	0.04
$Ba_3GdB_9O_{18}$ [42]	7.193 Å	8.603 Å	251 K	145 K	0.73
$Ba_3GdB_3O_9$ [44]	4.776 Å	7.710 Å	68 K	343 K	0.05

3.2. Magnetic Properties

To determine magnetic properties, pellets with a diameter of 3 mm and a height of 1 mm were prepared with 50% silver admixture. Figure 2 displays our data for the isothermal magnetization of the four different materials at temperatures between 0.4 and 10 K.

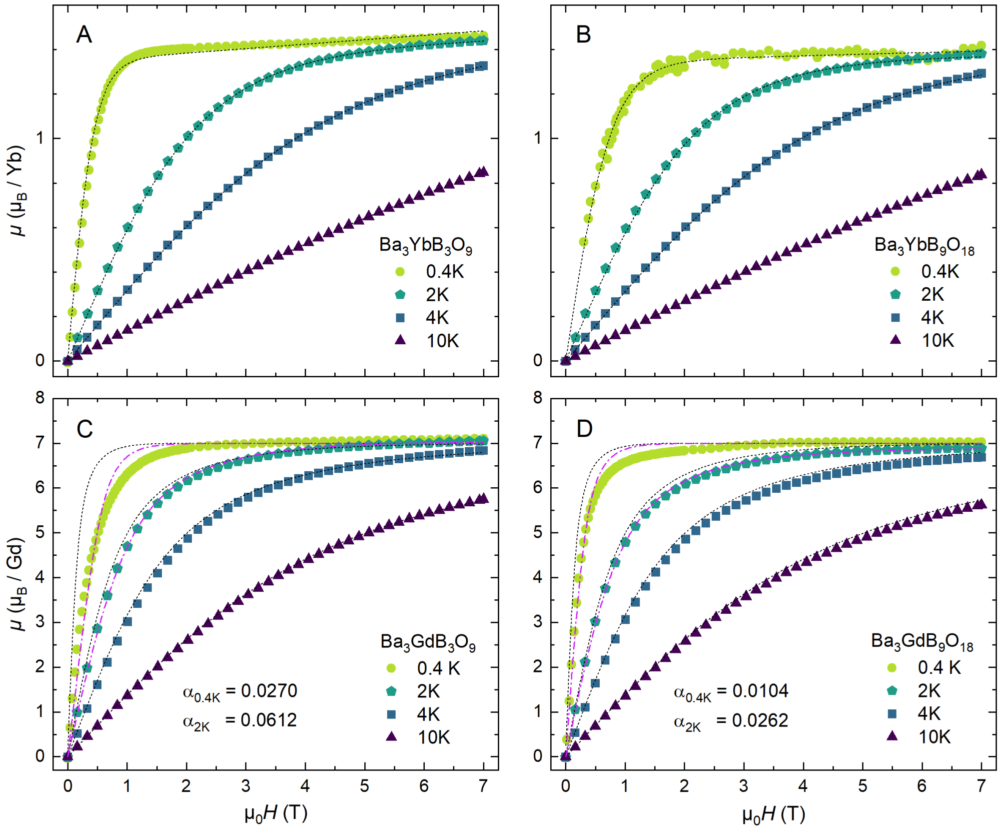

Figure 2. Magnetic moment μ in units of Bohr magneton μ_B per magnetic ion versus applied field H for different temperatures for $Ba_3YbB_3O_9$ (**A**), $Ba_3YbB_9O_{18}$ (**B**), $Ba_3GdB_3O_9$ (**C**), and $Ba_3GdB_9O_{18}$ (**D**). The black dotted lines show calculated moments from Equation (1) for a free ion. The dashed pink lines show a mean-field approximation according to Equation (2).

The magnetic moment of non-interacting dipoles can be described by the Brillouin function:

$$\mu(B) = gJ\left[\frac{2J+1}{2J}\coth\left(\frac{2J+1}{2J}\frac{g\mu_\mathrm{B}JB}{k_\mathrm{B}T}\right) - \frac{1}{2J}\coth\left(\frac{g\mu_\mathrm{B}B}{2k_\mathrm{B}T}\right)\right] + x_0B \tag{1}$$

with a total angular momentum of J and the Landé factor g. The function $\mu(B)$ (Equation (1)) was fitted to the data with fixed T and fixed $J = 7/2$ and $g = 2$ for the Gd compounds. A van Vleck contribution x_0B was also added, although this did not become dominant for any of the materials.

The ytterbium samples (Figure 2A,B) can be approximated as free-ion systems, as the magnetic interaction energies are very small compared to thermal energy at the studied temperatures. Note that their magnetic interaction is much smaller compared to their Gd counterparts due to the smaller effective moment. For these samples, saturation was achieved in the 0.4 K and 2 K measurements. Fitting Equation (1) yields a g factor of 2.71 for $Ba_3YbB_3O_9$ and 2.70 for $Ba_3YbB_9O_{18}$. Significant anisotropy of g has been observed previously for similar Yb compounds [48] and for $Ba_3YbB_3O_9$ by Bag et al. [38] ($g_{ab} = 2.19, g_c = 3.38$), but the polycrystalline average observed is in good agreement with reports by Cho et al. [39] ($g_\mathrm{PM} = 2.77(1)$).

Both gadolinium systems saturate close to the expected $\mu_\mathrm{sat} = 7\mu_\mathrm{B}$ for high fields and low temperatures, indicating the expected $g = 2$. Note that the single-ion approximation (black, Figure 2C,D) is inaccurate due to the interaction between ions for the data below 2 K. This manifests as a shift in the magnetic saturation to higher fields than expected in the free-ion model. This effect is enhanced in $Ba_3GdB_3O_9$ due to the higher magnetic moment density. Although the structural parameters are similar, the interaction in the gadolinium compounds is enhanced when compared to the ytterbium compounds, as the magnetic moments are significantly larger ($S_\mathrm{eff} = 1/2$ vs. $S = 7/2$). An increase in interactions upon rare-earth replacement has been observed in the isostructural $KBaYb(BO_3)_2$ [19] and $KBaGd(BO_3)_2$ [20] as well as in the iso structural $NaYbP_2O_7$ [21] and $NaGdP_2O_7$ [24]. Therefore, a mean-field approximation was conducted by fitting Equation (2) to the 2 K and 0.4 K gadolinium datasets (pink, Figure 2C,D):

$$\mu = \mu_\mathrm{sat}B_J\left[\frac{g\mu_\mathrm{B}J}{k_\mathrm{B}T}(H + \alpha\mu)\right]. \tag{2}$$

The mean-field model fits the data significantly better than the free-ion approximation; however, there are still significant deviations, likely due to crystal electric field (CEF) effects. For 2 K, the mean-field model fits significantly better than for 0.4 K. The mean-field parameter α appears to be temperature-dependent, as both samples exhibit a decrease in α for lower temperatures. This unexpected temperature dependence hints at influences that cannot be described well by the mean-field model—likely CEF effects and short-ranged magnetic correlations. For $Ba_3GdB_9O_{18}$, the onset of magnetic order could also play a role, even though this occurs at significantly lower temperatures.

The magnetic susceptibility χ of the samples was measured down to 0.4 K. For high temperatures, an external field of 7 T was applied, and for low temperatures, a low field of 5 mT was utilized. The inverse susceptibility was fitted with a modified Curie–Weiss function (Equation (3)) to obtain effective moments and Weiss temperature ([49] Equation (18)):

$$\chi^{-1} = (T - \Theta_\mathrm{W})\left[3k_\mathrm{B}\mu_0N_\mathrm{A}\mu_\mathrm{B}^2\mu_\mathrm{eff}^{-2} + \chi_0\right]. \tag{3}$$

For high temperatures, Yb and Gd samples show a linear relation between χ^{-1} and T. For $T < 100$ K, both Yb compounds deviate from the linear relation; as the CEF splits, the energy levels' occupation shifts [50]. At low temperatures and low magnetic fields, the Yb samples exhibit Kramers behavior, thus returning to a linear $\chi^{-1}(T)$. To obtain μ_{eff} and Θ_{W} for the Yb samples, Equation (3) was fitted between 100 K and 300 K, as shown in Figure 3. For $Ba_3YbB_3O_9$, the resulting effective moment of 4.73 μ_{B} and Weiss temperature of $\Theta_{\mathrm{W}} = -108\,\mathrm{K}$ are close to reports by Gao et al. [36] ($\mu_{\mathrm{eff}} = 4.60\,\mu_{\mathrm{B}}, \Theta_{\mathrm{W}} = -109\,\mathrm{K}$), as well as by Cho et al. [39] ($\mu_{\mathrm{eff}} = 4.89(1)\,\mu_{\mathrm{B}}, \Theta_{\mathrm{W}} = -105(1)\,\mathrm{K}$). For $Ba_3YbB_9O_{18}$, the effective moment of 4.75 μ_{B} and Weiss temperature $\Theta_{\mathrm{W}} = -100\,\mathrm{K}$ are close to data reported by Khatua et al. [40] ($\mu_{\mathrm{eff}} = 4.73\,\mu_{\mathrm{B}}, \Theta_{\mathrm{W}} = -90\,\mathrm{K}$), as well as by Cho et al. [39] ($\mu_{\mathrm{eff}} = 4.74(1)\,\mu_{\mathrm{B}}, \Theta_{\mathrm{W}} = -99(1)\,\mathrm{K}$). There is a small discrepancy compared to the observations by Liu et al. [41] ($\mu_{\mathrm{eff}} = 4.34\,\mu_{\mathrm{B}}, \Theta_{\mathrm{W}} = -78.09\,\mathrm{K}$), but this dataset was collected at 0.2 T, while our data was collected at a significantly higher field of 7 T. The resulting effective moments of 4.73 μ_{B} and 4.75 μ_{B} are close to the theoretical $\mu_{\mathrm{eff}} = g_J\sqrt{J(J+1)}\mu_{\mathrm{B}} = 4.54\,\mu_{\mathrm{B}}$ for a free Yb^{3+} ion with $J = 7/2$ and $g_J = 8/7$. The absolute values of the Weiss temperatures from the high-temperature fit of the two Yb materials cannot be interpreted as indicative of large coupling between the moments, because they result from the crystal field splitting, leaving only the low-lying doublet at low temperatures [36]. For $Ba_3YbB_9O_{18}$, the energy gap of the effective two-level system has been reported at $\Delta E/k_{\mathrm{B}} = 210.61\,\mathrm{K}$ [41].

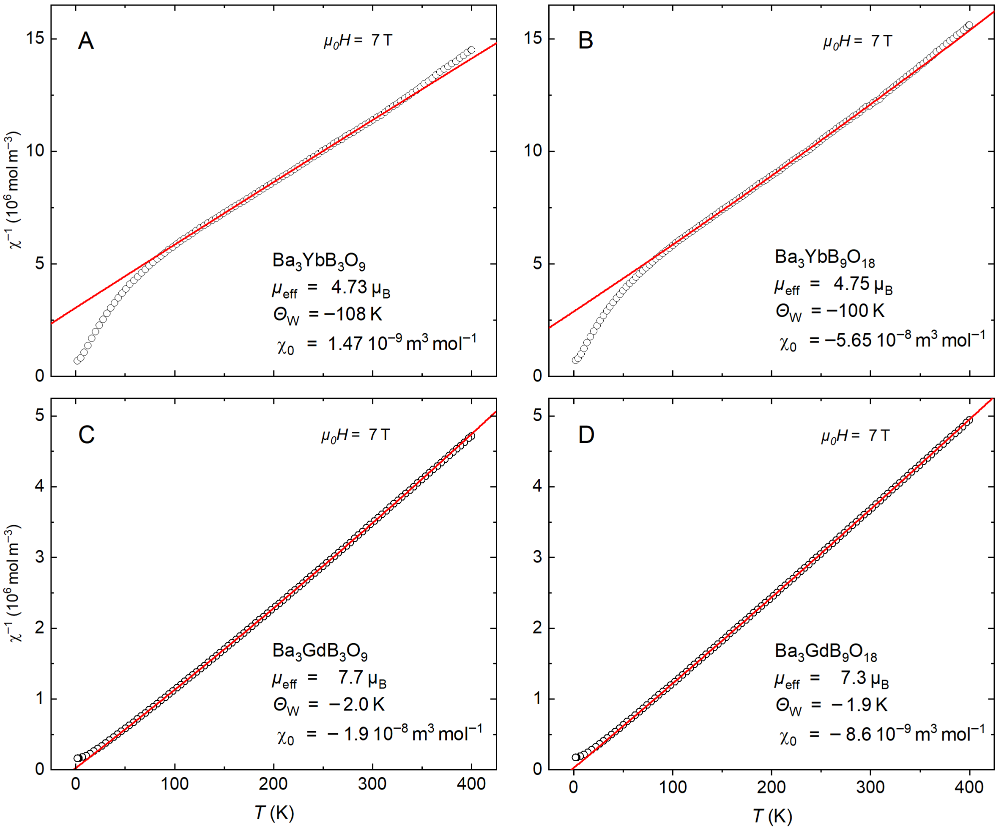

Figure 3. Inverse magnetic susceptibility at an applied field of 7 T and fitted with Equation (3), with the listed parameters for $Ba_3YbB_3O_9$ (**A**), $Ba_3YbB_9O_{18}$ (**B**), $Ba_3GdB_3O_9$ (**C**), and $Ba_3GdB_9O_{18}$ (**D**).

The Gd samples show a linear relation for $\chi^{-1}(T)$ down to approximately 25 K, when polarization of the moments starts to become significant; therefore, fitting was performed between 100 K and 350 K. The resulting effective moments are close to the theoretical $\mu_{\mathrm{eff}} = 7.94\,\mu_{\mathrm{B}}$. For $Ba_3GdB_3O_9$, the effective moment of 7.7 μ_{B} and Weiss temperature of $\Theta_{\mathrm{W}} = -2.0\,\mathrm{K}$ are comparable to reports on the similar frustrated oxide magnet $KBaGd(BO_3)_2$ by Sanders et al. [34] ($\mu_{\mathrm{eff}} = 7.70\,\mu_{\mathrm{B}}, \Theta_{\mathrm{W}} = -1.64\,\mathrm{K}$), as well as by Jesche et al. [20] ($\mu_{\mathrm{eff}} = 7.91\,\mu_{\mathrm{B}}, \Theta_{\mathrm{W}} = -1.4\,\mathrm{K}$). Notably, we observed a slightly negative

Θ_W even in the high-temperature fit. For $Ba_3GdB_9O_{18}$, the resulting effective moment of $7.3\,\mu_B$ is slightly lower than the theoretical value for a free-ion model. Even though the nearest-neighbor distances are quite large in this compound, the reduction in μ_{eff} could hint at interactions between the moments. The Weiss temperature of $\Theta_W = -1.9$ K is quite close to zero, indicating a weak antiferromagnetic exchange. These results also are in good agreement with other Gd^{3+} frustrated oxides [24]. All compounds exhibit negative Θ_W in the high-temperature fits, suggesting dominant antiferromagnetic interaction.

For low temperatures and low fields, the $\chi^{-1}(T)$ behavior of all samples is linear (Figure 4). The Yb compounds now indicate fluctuating $S = 1/2$ Kramers doublets with reduced μ_{eff} as compared to high temperatures.

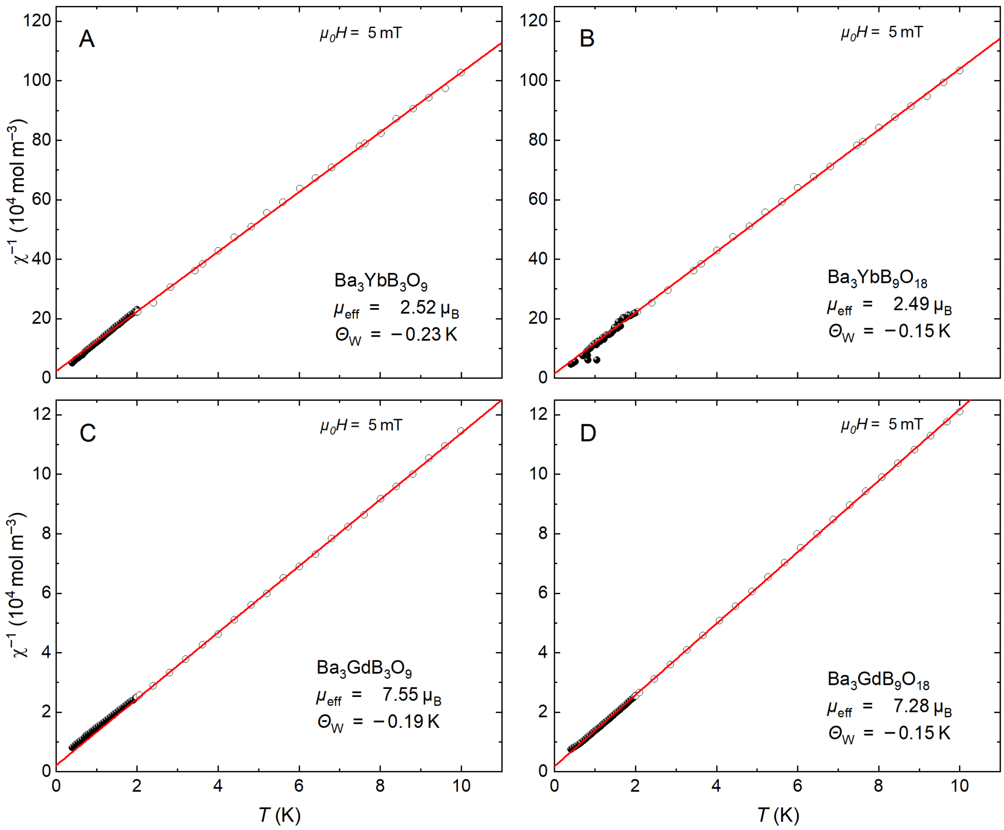

Figure 4. Inverse magnetic susceptibility at an applied field of 5 mT, with the listed parameters for $Ba_3YbB_3O_9$ (**A**), $Ba_3YbB_9O_{18}$ (**B**), $Ba_3GdB_3O_9$ (**C**), and $Ba_3GdB_9O_{18}$ (**D**). Empty symbols were measured with helium-4, filled symbols with helium-3. This data was fitted with Equation (3) with $\chi_0 = 0$ (red).

For $Ba_3YbB_3O_9$, the effective moment of $2.52\,\mu_B$ is very close to reports by Gao et al. [36] ($\mu_{eff} = 2.61\,\mu_B, \Theta_W = -2.3$ K), as well as by Cho et al. [39] ($\mu_{eff} = 2.56(1)\,\mu_B$, $\Theta_W = -0.24(1)$ K). The obtained Weiss temperature $\Theta_W = -0.23$ K is close to the results reported by Cho et al. [39], indicating very weak or highly frustrated interactions.

For $Ba_3YbB_9O_{18}$, the effective moment of $2.49\,\mu_B$ and Weiss temperature $\Theta_W = -0.15$ K are very close to data reported by Khatua et al. [40] ($\mu_{eff} = 2.32\,\mu_B, \Theta_W = -0.12$ K). Reports by Cho et al. [39] ($\mu_{eff} = 2.31(1)\,\mu_B, \Theta_W = -0.077(2)$ K) suggest a lower Θ_W but are based on measurements to 2 K.

Both Gd samples continue to exhibit a high effective magnetic moment of $7.55\,\mu_B$ and $7.28\,\mu_B$ at low temperatures. This is expected, as the full $S = 7/2$ multiplet contributes to the magnetic moment in Gd^{3+} ions [20,24,34].

Θ_W for all samples is increased in this temperature range but remains negative. This suggests antiferromagnetic behavior with a low ordering temperature T_N. Both $Ba_3XB_9O_{18}$ samples show higher Θ_W than their respective $Ba_3XB_3O_9$ counterparts. The increase in Θ_W corresponds to a lower magnetic moment density and, thus, reduced magnetic interactions. All compounds show no signs of long-range order down to the lowest observed temperatures.

3.3. Specific Heat

Specific heat was measured on the powder-pressed samples with silver admixture in the PPMS. The helium-3 data was scaled to the helium-4 data, and the contributions of silver as well as the phonons were subtracted. The phonon contribution was determined by fitting a combined Debye–Einstein model to the high-temperature data:

$$c_{\mathrm{ph}} = 3\gamma R N k_{\mathrm{B}} \left(\frac{\Theta_{\mathrm{E}}}{T}\right)^2 \frac{\exp\left(\frac{\Theta_{\mathrm{E}}}{T}\right)}{\left(\exp\left(\frac{\Theta_{\mathrm{E}}}{T}\right) - 1\right)^2} + 9(1-\gamma) R N k_{\mathrm{B}} \left(\frac{T}{\Theta_{\mathrm{D}}}\right)^3 \int_0^{\frac{\Theta_{\mathrm{D}}}{T}} \frac{x^3}{\exp x - 1} dx \quad (4)$$

with $x = \Theta_D/T$ and the mixing factor $0 \leq \gamma \leq 1$. The resulting parameters are listed in Table 2. These fits were solely created to obtain a description of the low-temperature phonon contribution to specific heat. Since the temperature range for fitting is very limited ($T \leq 30\,\mathrm{K}$), the obtained values of the Debye temperature Θ_D, the Einstein temperature Θ_E, and the mixing parameter γ have no intrinsic physical significance and should not be interpreted beyond their role in providing a convenient empirical description of the data. For low temperatures, the microcalorimeter measurements were extended below 600 mK by means of ADR warmup analysis. In this process, a pellet is allowed to warm up to the starting temperature T_0 after a magnetic cooldown under parasitic heat load. From this warming curve $T(t)$, the specific heat c_p can be calculated by

$$c_p = \frac{m_{\mathrm{mol}}}{m} \frac{dQ}{dT} = \frac{m_{\mathrm{mol}}}{m} \frac{dQ}{dt} \left(\frac{dT}{dt}\right)^{-1}. \quad (5)$$

It has previously been shown that, for the PPMS puck-based setup, the assumption of constant $\dot{Q}_{\mathrm{parasitic}}(T)$ holds for $20\,\mathrm{mK} < T < 1.5\,\mathrm{K}$ [20,24,30]. The specific heat from the ADR measurements was scaled to the zero field data measured by microcalorimetry to determine the heat load.

Magnetic specific heat c_m for a system of non-interacting magnetic dipoles in an external field can be described as follows ([51] Equation (9.15b)):

$$c_{\mathrm{m}} = \frac{x^2 R}{4} \sinh^{-2}\left(\frac{x}{2}\right) - \frac{x^2}{4}(2J+1)^2 \sinh^{-2}\left(\frac{x}{2}(2J+1)\right) \quad \text{with} \quad x = \frac{\mu_{\mathrm{B}} g H_{\mathrm{eff}}}{k_{\mathrm{B}} T}. \quad (6)$$

The contribution of internal fields and antiferromagnetic exchange was considered through an effective field H_{eff} at the position of each magnetic ion. This effective field was determined through fitting the specific heat peak. The values of H_{eff} were mostly lower than the applied field, which may be attributed to the antiferromagnetic exchange in the compounds, while a slightly enhanced effective field was used for $Ba_3GdB_9O_{18}$ at an applied field of 1 T. The specific heat data (Figure 5) was fitted with Equation (6). $Ba_3GdB_3O_9$ shows a clear maximum in specific heat that is shifted to higher temperatures with increased field. In zero field, a broad peak is also found, with no indication of a long-range ordered magnetic phase transition.

In a finite field, the molar specific heat of $Ba_3GdB_9O_{18}$ behaves similarly to that of $Ba_3GdB_3O_9$, as expected, also exhibiting a broad peak that is shifted to higher T with increasing field. The zero-field specific heat shows a clear phase transition anomaly at 108 mK, followed by a broader peak at 368 mK. The lambda-shaped peak could indicate antiferromagnetic order, given the negative sign of the Curie–Weiss temperature. The ordering occurs at a temperature close to but lower than $|\Theta_W| = 0.13\,\mathrm{K}$, which can be attributed to frustration in the magnetic lattice. There is also a small anomaly at elevated temperatures, which coincides with the magnetic ordering of the foreign phase $GdBO_3$. This has been previously reported at 1.72 K [52], which matches our observations of a contribution at 1.7 K.

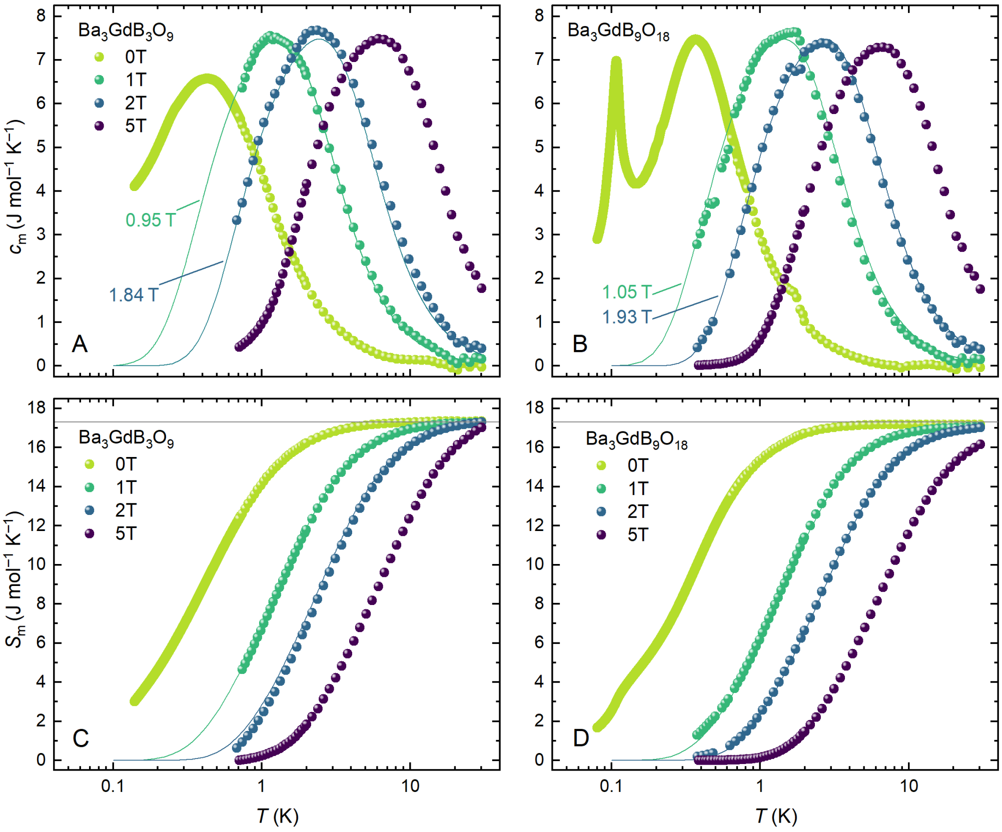

Figure 5. Specific heat and magnetic entropy for $Ba_3GdB_3O_9$(**A**,**C**) and $Ba_3GdB_9O_{18}$ (**B**,**D**) in various different fields. Colored lines display model calculations from Equation (6), with “effective” field values as indicated.

The origin of the absence of a magnetic transition in $Ba_3GdB_3O_9$ is unclear, as this material crystallizes in a different structure with two inequivalent Gd sites and chain motives. It can also not be excluded that an ordering would occur at temperatures lower than the minimal temperature of the ADR experiment.

From the measured specific heat data, magnetic entropy S_m was calculated using

$$S_m = S_0 + \int dT \frac{c_m}{T}. \tag{7}$$

The offset constant S_0 is necessary, as c_m is only available starting from finite T_{min}. This offset was determined from magnetization data at 2 K by

$$S_m = \mu_0 \int_{B_0}^{B_1} dH \frac{\partial M}{\partial T}. \tag{8}$$

The resulting magnetic entropy shows a clear saturation effect at the expected value of $R \ln 8 = 17.3\,\mathrm{J mol^{-1} K^{-1}}$. $Ba_3GdB_3O_9$ saturates at slightly lower temperatures for a given field when compared to $Ba_3GdB_9O_{18}$. The contribution to S_m of the lambda-like peak in c_m for $Ba_3GdB_9O_{18}$ is small when compared with the broader peak at higher temperatures. This clearly indicates that the ordered moment comprises only a low fraction of the total Gd moment.

3.4. Actual Refrigeration Performance

To ascertain the actual refrigeration performance of the compounds, the 15 mm pellets were individually mounted to the PPMS puck-based setup described in Section 2. This setup was isothermally magnetized to an applied field of 5 T at a starting temperature of 2 K. After magnetization, the remaining helium atmosphere was evacuated from the sample chamber, establishing near-adiabatic conditions. Subsequently, the field was fully ramped down at a rate of 5 mT/min. The sample temperature was recorded during the parasitic warming back to the sample chamber temperature (Figure 6). From the warmup curve $T(t)$, the refrigerant capacity q was calculated by integrating the known parasitic heat flow. This represents the amount of heat that the refrigerant can accept when warming to a specified temperature:

$$q(T) = \int_{t(T_{\min})}^{t(T)} \frac{dQ}{dt} dt'. \tag{9}$$

The median $\dot{Q}$ of all ADR runs was 63(8) nW. Figure 6 displays the warmup data for all studied materials. Table 3 provides an overview of the relevant parameters as well as a comparison to other refrigerants. The Yb compounds achieved the lowest ADR temperatures T_{ADR}, with $Ba_3YbB_3O_9$ attaining 40.0 mK and $Ba_3YbB_9O_{18}$ attaining 37.0 mK. This is comparable to values reported for other frustrated oxides like $KBaYb(BO_3)_2$ (Tokiwa et al., 40 mK [19]) or $NaYbP_2O_7$ (Arjun et al., 45 mK [21]). There is no indication for long-range magnetic order in the Yb compounds down to the minimum temperatures attained during ADR, corroborating previous measurements [37,38,44]. This suggests that the obtained minimal temperatures are limited by the non-perfect adiabaticity of the setup, and not yet by the vanishing entropy in zero field.

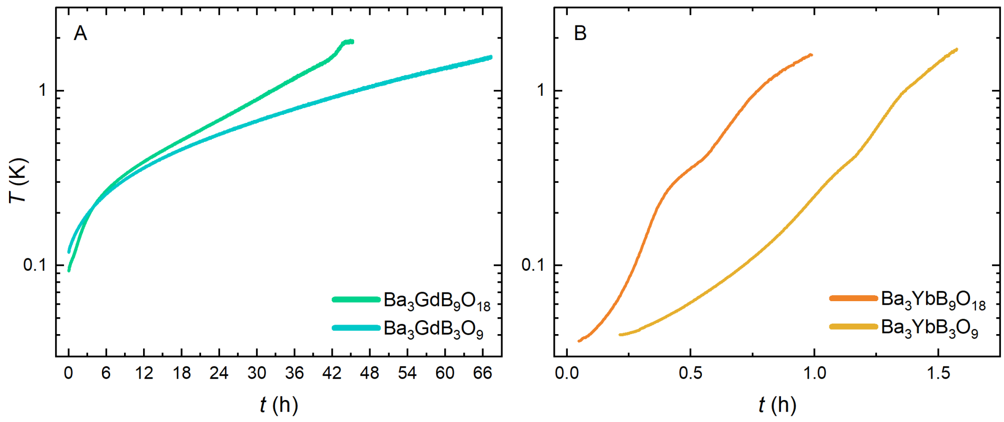

Figure 6. Temperature of samples during parasitic warmup after ADR: (**A**,**B**) show data for the Gd- and Yb-based compounds, respectively. The median total parasitic heat leak was $\dot{Q} = 63(8)$ nW for these measurements.

$Ba_3YbB_3O_9$ warms 60% slower than $Ba_3YbB_9O_{18}$, as expected, since the former has a 71% higher magnetic moment density and 82% higher magnetic entropy density compared to the latter. This is also reflected in the 120% enhanced refrigerant capacity q.

As expected from the fact that the Gd materials—compared to their Yb counterparts—feature a stronger magnetic interaction and, thus, reduced entropy at higher temperatures, they exhibit higher T_{ADR}, with $Ba_3GdB_3O_9$ attaining 119 mK and $Ba_3GdB_9O_{18}$ attaining

94.3 mK. While the difference in minimal temperature T_{ADR} is quite small for the two Yb compounds, at $\Delta T_{\mathrm{ADR,Yb}} = 3.0\,\mathrm{mK}$, the difference in minimal temperature is increased between the Gd materials, at $\Delta T_{\mathrm{ADR,Gd}} = 24.7\,\mathrm{mK}$. $Ba_3GdB_3O_9$ warms 60% slower to 2 K than $Ba_3GdB_9O_{18}$, compatible with the 56% higher entropy density. This is also reflected in the 105% higher refrigerant capacity q. All substances reached significantly lower temperatures T_{ADR} during the ADR than their respective $|\Theta_{\mathrm{W}}|$, with all except $Ba_3GdB_9O_{18}$ showing no signatures of long-range order. This suggests a possible impact of geometric frustration. However, more detailed study of the magnetic properties would be required to draw a clearer conclusion.

Table 3. Comparison of values for the effective magnetic moment and Curie–Weiss temperature (from Figure 4); minimal ADR temperature T_{ADR} for a full demagnetization from 2 K, 5 T, and subsequent warmup back to 2 K; refrigerant capacity q for a warmup from T_{ADR} back to 2 K; and full entropy density, calculated from the magnetic ion density, for the four different studied materials, together with results from the literature for $KBaYb(BO_3)_2$ and $KBaGd(BO_3)_2$.

Compound	μ_{eff}	Θ_{W}	T_{ADR}	q	ΔS_{m}
$Ba_3YbB_9O_{18}$	2.49 μ_{B}	−0.15 K	37.0 mK	0.84 $\mathrm{mJcm^{-3}}$	24.0 $\mathrm{mJK^{-1}cm^{-3}}$
$Ba_3YbB_3O_9$	2.52 μ_{B}	−0.23 K	40.0 mK	1.78 $\mathrm{mJcm^{-3}}$	43.6 $\mathrm{mJK^{-1}cm^{-3}}$
$KBaYb(BO_3)_2$ [19,25]	2.28 μ_{B}	−0.06 K	40 mK	-	57.95 $\mathrm{mJK^{-1}cm^{-3}}$
$Ba_3GdB_9O_{18}$	7.59 μ_{B}	−0.13 K	94.3 mK	29.4 $\mathrm{mJcm^{-3}}$	66.8 $\mathrm{mJK^{-1}cm^{-3}}$
$Ba_3GdB_3O_9$	7.55 μ_{B}	−0.19 K	119.2 mK	56.0 $\mathrm{mJcm^{-3}}$	104 $\mathrm{mJK^{-1}cm^{-3}}$
$KBaGd(BO_3)_2$ [20,25]	7.55 μ_{B}	−0.55 K	122 mK	-	139 $\mathrm{mJK^{-1}cm^{-3}}$

To compare the refrigeration performance of various materials, the change in the volumetric magnetic entropy density $\Delta S = S_{B=0} - S_{B_i}$ was calculated for an initial field of 5 T (Figure 7A). Likewise, the refrigerant capacity q was calculated according to Equation (9) for a demagnetization from $B_i = 5\,\mathrm{T}$ (Figure 7B). This indicates the amount of heat that the refrigerant can absorb during warmup to a specified temperature—in this case, 2 K.

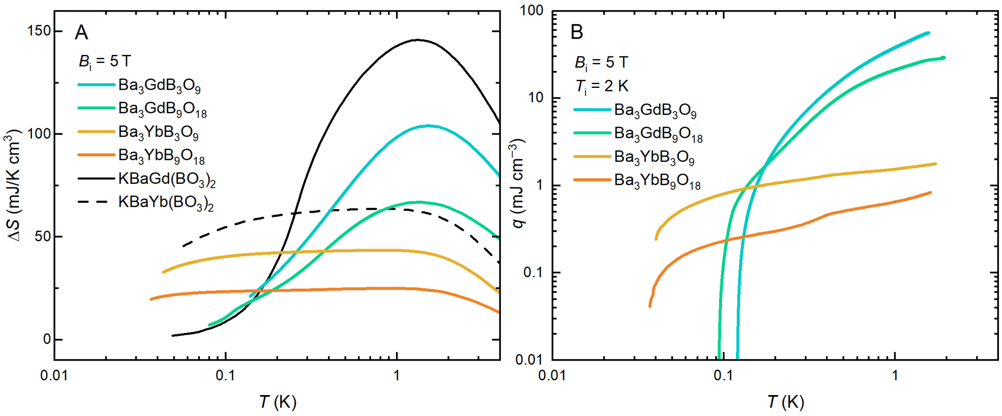

Figure 7. Volumetric entropy increment $\Delta S(T) = S(T,0) - S(T,B_i)$ with $B_i = 5\,\mathrm{T}$ (**A**), as well as refrigerant capacity q ((**B**), see text), for different studied Yb and Gd borates vs. temperature.

In terms of entropy change (Figure 7A), the Yb (blue, green) and Gd (orange, yellow) compounds differ in magnitude as well as temperature distribution. As expected, the Gd-based substances offer significantly higher entropy lift per unit volume, with $Ba_3YbB_3O_9$ outperforming $Ba_3YbB_9O_{18}$ due to its higher moment density. However, $\Delta S(T)$ shows a peak for these substances; this can be interpreted as representing the optimal operating conditions. Meanwhile, the Yb compounds offer a far broader plateau in $\Delta S(T)$, albeit at a significantly reduced magnitude. The tendency for Yb-based refrigerants to offer optimal performance over a wider temperature range has been observed for multiple mK refrigerants [25].

In comparison to the previously studied borates $KBaYb(BO_3)_2$ and $KBaGd(BO_3)_2$, the performance of the new refrigerants is limited [19,20,25]. $KBaYb(BO_3)_2$ (Figure 7A, dashed line) offers higher ΔS than $Ba_3YbB_3O_9$ and $Ba_3YbB_9O_{18}$ over the entire temperature range. $Ba_3GdB_3O_9$ and $Ba_3GdB_9O_{18}$ outperform $KBaGd(BO_3)_2$ (Figure 7A, solid line) for very low temperatures ($T < 0.14\,\mathrm{K}$ and $T < 0.17\,\mathrm{K}$) but offer only limited entropy lift at higher temperatures. This can be explained by the higher magnetic moment density in the diborates when compared to the triborates studied here. Overall, enhanced magnetic moment density combined with strong frustration seems to be preferable to more diluted frustrated systems for refrigeration purposes.

4. Conclusions

Magnetic measurements, specific heat, and ADR results for $Ba_3YbB_3O_9$, $Ba_3YbB_9O_{18}$, $Ba_3GdB_3O_9$, and $Ba_3GdB_9O_{18}$ are presented in this study. All of the materials exhibit slightly negative Θ_W, indicating weak antiferromagnetic interactions, which are stronger in case of the Gd materials due to their larger moment size. Magnetization of the ytterbium samples adhered closely to the single-ion model, while the gadolinium systems necessitated a mean-field approach. The susceptibility data reveals paramagnetic behavior to 0.4 K, underpinned by specific heat data clearly exhibiting a Schottky-type anomaly.

Major MCE was observed in all substances during a demagnetization from 2 K, 5 T. Both $Ba_3GdB_9O_{18}$ and $Ba_3GdB_3O_9$ achieved low ADR temperatures for gadolinium systems, while $Ba_3YbB_9O_{18}$ and $Ba_3YbB_3O_9$ were competitive with other rare-earth oxide quantum magnets with regard to temperature. All compounds offered significantly lower entropy densities and refrigerant capacities than the benchmark borates $KBa(Gd, Yb)(BO_3)_2$. For $Ba_3GdB_9O_{18}$, the formation of long-range magnetic order was observed by means of ADR warmup analysis. The specific heat exhibited a clear lambda-shaped phase transition anomaly in zero field, followed by a broad maximum at higher temperatures. Data in 1 T are well described by a $S = 7/2$ Schottky anomaly. Long-range order was not detected in $Ba_3GdB_3O_9$, even though this compound has a higher magnetic moment density. The absence of magnetic order in $Ba_3GdB_3O_9$ is likely caused by frustration due to the trigonal lattice. It also has to be considered that this material has two nonequivalent magnetic sites.

Both $Ba_3YbB_9O_{18}$ and $Ba_3YbB_3O_9$ attain low temperatures during demagnetization when compared to other frustrated Yb-based quantum magnets. While they are competitive with regard to temperature, they lack in terms of refrigerant capacity and entropy density when compared to incumbents like $KBaYb(BO_3)_2$.

Author Contributions: P.G. and A.J. designed the study; T.T. and F.K. synthesized the samples; T.T. and F.K. performed the structural, magnetic, and thermodynamic characterization measurements; T.T., C.H., M.K. and F.K. performed the ADR experiments; M.K., A.K. and P.G. wrote the manuscript with input from all co-authors. All authors have read and agreed to the published version of the manuscript.

Funding: The work was supported by the Deutsche Forschungsgemeinschaft (DFG, German Research Foundation), Grants No. 514162746 (GE 1640/11–1) and No. TRR 360–492547816.

Data Availability Statement: Data associated with this manuscript are available from Zenodo (https://doi.org/10.5281/zenodo.17855051, uploaded on 6 December 2025).

Conflicts of Interest: The authors declare no conflicts of interest.

Abbreviations

The following abbreviations are used in this manuscript:

ADR	Adiabatic demagnetization refrigeration
CEF	Crystal electric field
DR	Dilution refrigerator
MCE	Magnetocaloric effect
PPMS	Physical Property Measurement System
VSM	Vibrating-sample magnetometer
XRD	X-ray diffraction

References

1. Cao, H. Refrigeration Below 1 Kelvin. *J. Low Temp. Phys.* **2021**, *204*, 175–205. [CrossRef]
2. London, H.; Clarke, G.R.; Mendoza, E. Osmotic Pressure of He^3 in Liquid He^4, with Proposals for a Refrigerator to Work below 1°K. *Phys. Rev.* **1962**, *128*, 1992–2005. [CrossRef]
3. Pobell, F. The ^3He–^4He Dilution Refrigerator. In *Matter and Methods at Low Temperatures*, 3rd ed.; Springer: Berlin/Heidelberg, Germany, 2007; pp. 149–189. [CrossRef]
4. Zhao, Z. Cryogen-Free Dilution Refrigerator Systems. In *Cryogenic Engineering and Technologies*; CRC Press: Boca Raton, FL, USA, 2019.
5. Esat, T.; Borgens, P.; Yang, X.; Coenen, P.; Cherepanov, V.; Raccanelli, A.; Tautz, F.S.; Temirov, R. A Millikelvin Scanning Tunneling Microscope in Ultra-High Vacuum with Adiabatic Demagnetization Refrigeration. *Rev. Sci. Instruments* **2021**, *92*, 063701. [CrossRef] [PubMed]
6. Chen, Z.; Shen, J.; Zhao, Y.; Zheng, W.; Yang, L.; Lu, Y.; Liu, J.; Li, Z. Experimental Research on a High Efficiency Adiabatic Demagnetization Refrigerator. *Appl. Therm. Eng.* **2025**, *265*, 125562. [CrossRef]
7. Xu, Q.F.; Wu, R.T.; Long, L.S.; Zheng, L.S. Ultralow-Temperature Magnetic Refrigeration Inorganic Materials: From Designed Synthesis to Adiabatic Demagnetization Refrigeration. *Acc. Chem. Res.* **2025**, *58*, 2898–2909. [CrossRef] [PubMed]
8. Shirron, P.J.; Kimball, M.O.; Wegel, D.C.; Canavan, E.R.; DiPirro, M.J. Design of a 3-Stage ADR for the Soft x-Ray Spectrometer Instrument on the ASTRO-H Mission. In Proceedings of the SPIE Astronomical Telescopes + Instrumentation, San Diego, CA, USA, 27 June–2 July 2010 p. 773212. [CrossRef]
9. Shirron, P. Optimization Strategies for Single-Stage, Multi-Stage and Continuous ADRs. *Cryogenics* **2014**, *62*, 140–149. [CrossRef]
10. Shirron, P.J.; Kimball, M.O.; James, B.L.; Muench, T.; Canavan, E.R.; DiPirro, M.J.; Bialas, T.A.; Sneiderman, G.A.; Boyce, K.R.; Kilbourne, C.A.; et al. Design and On-Orbit Operation of the Adiabatic Demagnetization Refrigerator on the Hitomi Soft X-Ray Spectrometer Instrument. Number GSFC-E-DAA-TN51681. In Proceedings of the SPIE Astronomical Telescopes + Instrumentation 2018, Austin, TX, USA, 10–15 June 2018.
11. Duval, J.M.; Prouvé, T.; Shirron, P.; Shinozaki, K.; Sekimoto, Y.; Hasebe, T.; Vermeulen, G.; André, J.; Hasumi, M.; Montier, L.; et al. LiteBIRD Cryogenic Chain: 100 mK Cooling with Mechanical Coolers and ADRs. *J. Low Temp. Phys.* **2020**, *199*, 730–736. [CrossRef]
12. Paixao Brasiliano, D.A.; Duval, J.M.; Marin, C.; Bichaud, E.; Brison, J.P.; Zhitomirsky, M.; Luchier, N. YbGG Material for Adiabatic Demagnetization in the 100 mK–3 K Range. *Cryogenics* **2020**, *105*, 103002. [CrossRef]
13. Kleinhans, M.; Eibensteiner, K.; Leiner, J.; Resch, C.; Worch, L.; Wilde, M.; Spallek, J.; Regnat, A.; Pfleiderer, C. Magnetocaloric Properties of $R_3Ga_5O_{12}$ (R = Tb, Gd, Nd, Dy). *Phys. Rev. Appl.* **2023**, *19*, 014038. [CrossRef]
14. He, X.; Tian, L.; Gong, J.; Gao, X.; Liu, G.; Mo, Z. Novel Gadolinium Garnet $Gd_3Te_2Li_3O_{12}$: Magnetism and Magnetocaloric Performance for Sub-Kelvin Cryogenic Applications. *Dalton Trans.* **2025**, *54*, 9739–9748. [CrossRef]
15. Tokiwa, Y.; Piening, B.; Jeevan, H.S.; Bud'ko, S.L.; Canfield, P.C.; Gegenwart, P. Super-Heavy Electron Material as Metallic Refrigerant for Adiabatic Demagnetization Cooling. *Sci. Adv.* **2016**, *2*, e1600835. [CrossRef] [PubMed]
16. Gruner, T.; Chen, J.; Jang, D.; Banda, J.; Geibel, C.; Brando, M.; Grosche, F.M. Metallic Local-Moment Magnetocalorics as a Route to Cryogenic Refrigeration. *Commun. Mater.* **2024**, *5*, 63. [CrossRef]
17. Shimura, Y.; Yokoo, R.; Watanabe, K.; Furuie, H.; Tsujii, N.; Umeo, K.; Onimaru, T. $YbCo_2$: Large Magnetic Entropy Change per Volume in Yb-based Metallic Magnetic Refrigerants for Sub-Kelvin Temperature. *Appl. Phys. Lett.* **2025**, *127*, 102403. [CrossRef]
18. Zhang, X.; Zhang, T.; Zhuang, Z.; Leng, Z.; Wei, Z.; Liu, X.; Xiang, J.; Zhang, S.; Sun, P. $YbNi_4Mg$: Superheavy Fermion with Enhanced Wilson Ratio and Magnetocaloric Effect. *Phys. Rev. Mater.* **2025**, *9*, 014402. [CrossRef]
19. Tokiwa, Y.; Bachus, S.; Kavita, K.; Jesche, A.; Tsirlin, A.A.; Gegenwart, P. Frustrated Magnet for Adiabatic Demagnetization Cooling to Milli-Kelvin Temperatures. *Commun. Mater.* **2021**, *2*, 42. [CrossRef]

20. Jesche, A.; Winterhalter-Stocker, N.; Hirschberger, F.; Bellon, A.; Bachus, S.; Tokiwa, Y.; Tsirlin, A.A.; Gegenwart, P. Adiabatic Demagnetization Cooling Well below the Magnetic Ordering Temperature in the Triangular Antiferromagnet $KBaGd(BO_3)_2$. *Phys. Rev. B* **2023**, *107*, 104402. [CrossRef]
21. Arjun, U.; Ranjith, K.; Jesche, A.; Hirschberger, F.; Sarma, D.; Gegenwart, P. Efficient Adiabatic Demagnetization Refrigeration to below 50 mK with Ultrahigh-Vacuum-Compatible Ytterbium Diphosphates $AYbP_2O_7$ (A = Na, K). *Phys. Rev. Appl.* **2023**, *20*, 014013. [CrossRef]
22. Koskelo, E.C.; Mukherjee, P.; Liu, C.; Sackville Hamilton, A.C.; Ong, H.S.; Castelnovo, C.; Zhitomirsky, M.; Dutton, S.E. Comparative Study of Magnetocaloric Properties for Gd^{3+} Compounds with Different Frustrated Lattice Geometries. *PRX Energy* **2023**, *2*, 033005. [CrossRef]
23. Lin, J.; Wu, S.; Sun, K.; Li, H.F.; Chen, W.; Zhang, Y.; Li, L. Structural, Magnetic, and Magnetocaloric Characterizations of Geometrically-Frustrated $SrRE_2O_4$ (RE = Gd, Dy, Ho, Er) Oxides low-temperature cooling applications. *Eram. Int.* **2024**, *50*, 51269–51277. [CrossRef]
24. Telang, P.; Treu, T.; Klinger, M.; Tsirlin, A.A.; Gegenwart, P.; Jesche, A. Adiabatic Demagnetization Refrigeration with Antiferromagnetically Ordered $NaGdP_2O_7$. *Phys. Rev. B* **2025**, *111*, 064431. [CrossRef]
25. Treu, T.; Klinger, M.; Oefele, N.; Telang, P.; Jesche, A.; Gegenwart, P. Utilizing Frustration in Gd- and Yb-based Oxides for Milli-Kelvin Adiabatic Demagnetization Refrigeration. *J. Phys. Condens. Matter* **2025**, *37*, 013001. [CrossRef]
26. Berardi, F.; Nagle-Cocco, L.A.V.; Steele, J.M.A.; Zhang, X.; Liu, C.; Fischer, H.E.; Dutton, S.E. Structural Phase Transitions and Magnetic Characterization of Ba_2GdNbO_6 for Low-Temperature Magnetocaloric Refrigeration. *Chem. Mater.* **2025**. [CrossRef] [PubMed]
27. Channarayappa, S.K.; C., P.; Ranaut, D.; Saravanan, M.; Jaiswal-Nagar, D. Enhanced Adiabatic Demagnetization Cooling Performance in Exchange Frustrated $GdCrTiO_5$. *Phys. Rev. Appl.* **2025**, *23*, 014041. [CrossRef]
28. Cui, Y.; Wu, Z.; Sun, Z.; Du, K.; Luo, J.; Li, S.; Yang, J.; Wang, J.; Zhou, R.; Chen, Q.; et al. Spin-Supersolidity Induced Quantum Criticality and Magnetocaloric Effect in the Triangular-Lattice Antiferromagnet $Rb_2Co(SeO_3)_2$. *arXiv* **2025**. [CrossRef]
29. Lin, W.; Zhao, N.; Li, Z.; An, W.; Guo, R.; Wang, J.; Pan, C.; Wen, B.; Sheng, J.; Wu, L.; et al. Quantum Fluctuation-enhanced Milli-Kelvin Magnetic Refrigeration in Triangular Lattice Magnet $GdBO_3$. *arXiv* **2025**. [CrossRef]
30. Wang, Z.; Cui, X.; Treu, T.; Guo, J.; Liu, X.; Klinger, M.; Heil, C.; Ma, N.; Sheng, X.; Deng, Z.; et al. Antiferromagnetic Ordering and Critical Behavior Induced Giant Magnetocaloric Effect in Distorted Kagome Lattice Gd_3BWO_9. *Phys. Rev. Mater.* **2025**, *9*, 094407. [CrossRef]
31. Wan, T.; Wang, H.; Chen, Z.; Wang, Y.; Tu, H.; Li, Z.; Zhao, Y.; Shen, J.; Mo, Z.; Zhang, G. Magnetocaloric Effect in Gd8P2O17 and Gd3PO7. *Cryogenics* **2025**, *152*, 104198. [CrossRef]
32. Xu, Q.F.; Liu, X.Y.; Wu, R.T.; Fu, M.Y.; Chen, M.T.; Xiang, J.S.; Meng, Y.S.; Liu, T.; Sun, P.J.; Long, L.S.; et al. Temperature Below 30 mK Achieved by Adiabatic Demagnetization Refrigeration. *J. Am. Chem. Soc.* **2025**, *147*, 27089–27094. [CrossRef]
33. Yao, J.; Ren, W.; Guo, Q.; Liu, P.; Guan, Z.; Bao, C.; Zhang, Z.; Huang, D.; Zhang, K.; Wang, Y.; et al. Low-Field-Driven Giant Magnetocaloric Effect in $KGdF_4$ for Sub-Kelvin Cryogenic Refrigeration. *Mater. Today Phys.* **2025**, *55*, 101762. [CrossRef]
34. Sanders, M.B.; Cevallos, F.A.; Cava, R.J. Magnetism in the $KBaRE(BO_3)_2$ (RE = Sm, Eu, Gd, Tb, Dy, Ho, Er, Tm, Yb, Lu) Series: Materials with a Triangular Rare Earth Lattice. *Mater. Res. Express* **2017**, *4*, 036102. [CrossRef]
35. Pan, B.L.; Ni, J.M.; He, L.P.; Yu, Y.J.; Xu, Y.; Li, S.Y. Specific heat and thermal conductivity of the triangular-lattice rare-earth material $KBaYb(BO_3)_2$ at ultralow temperature. *Phys. Rev. B* **2021**, *103*, 104412. [CrossRef]
36. Gao, Y.; Xu, L.; Tian, Z.; Yuan, S. Synthesis and Magnetism of $RE(BaBO_3)_3$ (RE=Dy, Ho, Er, Tm, Yb) Series with Rare Earth Ions on a Two Dimensional Triangle-Lattice. *J. Alloy Compd.* **2018**, *745*, 396–400. [CrossRef]
37. Zeng, K.Y.; Ma, L.; Gao, Y.X.; Tian, Z.M.; Ling, L.S.; Pi, L. NMR study of the spin excitations in the frustrated antiferromagnet $Yb(BaBO_3)_3$ with a triangular lattice. *Phys. Rev. B* **2020**, *102*, 045149. [CrossRef]
38. Bag, R.; Ennis, M.; Liu, C.; Dissanayake, S.E.; Shi, Z.; Liu, J.; Balents, L.; Haravifard, S. Realization of quantum dipoles in triangular lattice crystal $Ba_3Yb(BO_3)_3$. *Phys. Rev. B* **2021**, *104*, L220403. [CrossRef]
39. Cho, H.; Blundell, S.J.; Shiroka, T.; MacFarquharson, K.; Prabhakaran, D.; Coldea, R. Studies on Novel Yb-based Candidate Triangular Quantum Antiferromagnets: $Ba_3YbB_3O_9$ and $Ba_3YbB_9O_{18}$. *arXiv* **2021**. [CrossRef]
40. Khatua, J.; Pregelj, M.; Elghandour, A.; Jagličic, Z.; Klingeler, R.; Zorko, A.; Khuntia, P. Magnetic Properties of the Triangular-Lattice Antiferromagnets $Ba_3RB_9O_{18}$ (R = Yb, Er).*Phys. Rev. B* **2022**, *106*, 104408. [CrossRef]
41. Liu, W.; Gao, Y.; Li, Y.; Li, Y.; Ren, W.; Sun, X.; Li, X.; Wang, M. Synthesis, Structure, Magnetism of Two-Dimensional Triangular Lattice Materials $Ba_3REB_9O_{18}$ (RE = Dy, Ho, Er, Tm and Yb). *J. Supercond. Nov. Magn.* **2025**, *38*, 231. [CrossRef]
42. Kabekkodu, S.N.; Dosen, A.; Blanton, T.N. PDF-5+: A Comprehensive Powder Diffraction File™ for Materials Characterization. *Powder Diffr.* **2024**, *39*, 47–59. [CrossRef]
43. Ilyukhin, A.B.; Dzhurinskij, B.F. Crystal structures of double borates $LnBa_3(BO_3)_3$ (Ln Dy, Ho, Tm, Yb, Lu). *Zhurnal Neorg. Khimii* **1993**, *38*, 1625–1630.

44. Khamaganova, T.N.; Kuperman, N.M.; Bazarova, Z.G. The Double Borates $Ba_3Ln(BO_3)_3$, *Ln* = La–Lu , Y. *J. Solid State Chem.* **1999**, *145*, 33–36. [CrossRef]
45. Kelly, N.D.; Le, M.D.; Sheptyakov, D.; Tacconis, C.; Liu, C.; Stenning, G.B.G.; Baker, P.J.; Dutton, S.E. Low-Temperature Magnetic Behavior on the Triangular Lattice in Hexagonal $Ba_3Tb(BO_3)_3$. *Phys. Rev. B* **2025**, *111*, 054427. [CrossRef]
46. Bera, A.K.; Lake, B.; Stein, W.D.; Zander, S. Magnetic Correlations of the Quasi-One-Dimensional Half-Integer Spin-Chain Antiferromagnets $SrM_2V_2O_8$ (*M* = Co, Mn). *Phys. Rev. B* **2014**, *89*, 094402. [CrossRef]
47. Zhou, J.; Shi, T.; Huang, R.T.; Liu, A.D.; Gong, G.S.; Wang, Y.Q.; Ling, L.S.; Li, J.X.; Han, Y.Y.; Tong, W.; et al. A Family of Quasi-One-Dimensional Zigzag Spin-Chain $Ba_2REV_3O_{11}$ (RE = Pr, Nd, and Gd–Ho) Compounds. *J. Mater. Chem. C* **2025**, *13*, 16040–16051. [CrossRef]
48. Ma, Z.; Wang, J.; Dong, Z.Y.; Zhang, J.; Li, S.; Zheng, S.H.; Yu, Y.; Wang, W.; Che, L.; Ran, K.; et al. Spin-Glass Ground State in a Triangular-Lattice Compound $YbZnGaO_4$. *Phys. Rev. Lett.* **2018**, *120*, 087201. [CrossRef]
49. Bałanda, M.; Dubiel, S.M.; Pełka, R. *Molecular Magnetic Materials*; John Wiley & Sons, Ltd.: Hoboken, NJ, USA, 2017; Chapter 1, pp. 1–28. [CrossRef]
50. Sala, G.; Stone, M.B.; Rai, B.K.; May, A.F.; Parker, D.S.; Halász, G.B.; Cheng, Y.Q.; Ehlers, G.; Garlea, V.O.; Zhang, Q.; et al. Crystal Field Splitting, Local Anisotropy, and Low-Energy Excitations in the Quantum Magnet $YbCl_3$. *Phys. Rev. B* **2019**, *100*, 180406. [CrossRef]
51. Pobell, F. Refrigeration by Adiabatic Demagnetization of a Paramagnetic Salt. In *Matter and Methods at Low Temperatures*, 3rd ed.; Springer: Berlin/Heidelberg, Germany, 2007; pp. 203–213. [CrossRef]
52. Mukherjee, P.; Wu, Y.; Lampronti, G.; Dutton, S. Magnetic Properties of Monoclinic Lanthanide Orthoborates, $LnBO_3$, Ln = Gd, Tb, Dy, Ho, Er, Yb. *Mater. Res. Bull.* **2018**, *98*, 173–179. [CrossRef]

https://doi.org/10.3390/app16010290